Medical Physics
The International Journal of Medical Physics Research and Practice

Accurate condensed history Monte Carlo simulation of electron transport. I. EGSnrc, the new EGS4 version

I. Kawrakow

Citation: Medical Physics **27**, 485 (2000); doi: 10.1118/1.598917
View online: http://dx.doi.org/10.1118/1.598917
View Table of Contents: http://scitation.aip.org/content/aapm/journal/medphys/27/3?ver=pdfcov
Published by the American Association of Physicists in Medicine

Accurate condensed history Monte Carlo simulation of electron transport. I. EGSnrc, the new EGS4 version

I. Kawrakow
National Research Council, Ottawa, ON K1A 0R6, Canada

(Received 10 March 1999; accepted for publication 8 December 1999)

In this report a new EGS4 version, called EGSnrc to reflect the substantial changes made to the original code is reported, which incorporates a new any-angle multiple elastic scattering theory, an improved electron-step algorithm, a correct implementation of the fictitious cross section method for sampling distances between discrete interactions, a more accurate evaluation of energy loss, as well as an exact boundary crossing algorithm. It is demonstrated that EGSnrc allows for an artifact free Monte Carlo simulation of ion chamber response and backscattering, situations that have been considered in the past as the two of the most stringent tests of condensed history Monte Carlo codes. A detailed discussion of the effect of the various components of the condensed history simulation of electron transport on the simulated ion chamber response is given in the accompanying paper. © *2000 American Association of Physicists in Medicine.* [S0094-2405(00)00803-8]

Key words: Monte Carlo simulations, EGSnrc, EGS4/PRESTA, condensed history technique

I. INTRODUCTION

The transport problem of particles in matter can be solved exactly, within the existing knowledge of the elementary collision processes, by the Monte Carlo technique. Monte Carlo simulations of particle transport processes are a faithful simulation of physical reality: particles are ''born'' according to distributions describing the source, they travel certain distances, determined by a probability distribution depending on the total interaction cross section, to the site of a collision and scatter into another energy and/or direction according to the corresponding differential cross section. This procedure is continued until the particle is absorbed or leaves the geometry under consideration. Quantities of interest can be calculated by averaging over a given set of Monte Carlo particle ''histories.'' The statistical uncertainty of the calculation depends on N, the number of particle histories simulated, and usually decreases as $N^{-1/2}$. Depending on the desired accuracy and/or the complexity and size of the geometry, this may lead to very long calculation times.

An additional difficulty occurs in the case of the simulation of electron transport. In the process of slowing down, a typical fast electron and the secondary particles it creates undergo hundreds of thousands of interactions with surrounding matter. Because of this large number of collisions, an event-by-event simulation of electron transport is often not possible due to limitations in computing power. To circumvent this difficulty, Berger[1] developed the ''condensed history'' (CH) technique. In this method, large numbers of transport and collision processes are ''condensed'' to a single electron step. The cumulative effect of the individual interactions is taken into account by sampling the change of the particle's energy and direction of motion at the end of the step from appropriate multiple scattering distributions. The CH technique, motivated by the fact that single collisions with the atoms cause, in most cases, only minor changes in the particle's energy and direction of flight, made the Monte Carlo (MC) simulation of charged particle transport possible but introduced an artificial parameter, the step length. The dependence of the calculated result on the step length has become known as a step-size artifact.[2]

In this report we discuss the accurate implementation of the CH technique. The developments presented here are implemented into the EGS4 system.[3] The resulting new EGS4 version will be referred to as EGSnrc to reflect the substantial changes made to the original code. Results of EGSnrc calculations of ion chamber response and backscattering, two situations where particularly strong step-size dependencies have been observed in the past, will be presented in Sec. III. These calculations demonstrate that EGSnrc allows for an artifact-free CH simulation of electron transport. A detailed discussion of the effect of the various components of the condensed history simulation of electron transport on the simulated ion chamber response is given in the accompanying paper (referred to in the following as paper II), which demonstrates the importance of the developments presented in the next section.

Improvements of the underlying cross sections are left for future developments of the system.

II. THE CH TECHNIQUE

M. Berger defined two basic classes of CH implementations.[1] In a class I scheme, particles move on a predetermined energy loss grid. Although such a scheme has the potential for a more accurate treatment of multiple elastic scattering, there are some disadvantages associated with the lack of correlation between energy loss and secondary particle production, as well as the necessity for difficult interpolations when the particle steps do not conform to the predetermined grid (e.g., because of interfaces and/or energy loss straggling). A class I scheme is implemented into ETRAN,[1,4] ITS,[5] or the electron component of MCNP.[6]

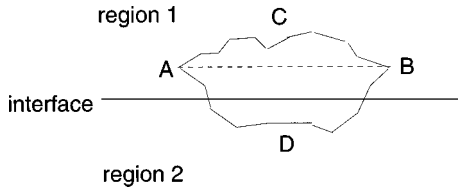

FIG. 1. The interface problem in the CH simulation of electron transport.

In a class II scheme, inelastic collisions resulting in the emission of bremsstrahlung above a given energy threshold E_γ and delta particles above E_δ are treated explicitly by creation and transport. Such interactions will be referred to in what follows as ''catastrophic'' or discrete interactions. Subthreshold processes are accounted for in a continuous-slowing-down-approximation (CSDA) model (although this is not a necessary requirement). A class II scheme is implemented in EGS4.[3]

Every implementation of the CH technique must define a procedure for the selection of the quantities determining a CH step. These quantities are the following.

(1) The step length s.

(2) The direction change due to multiple elastic scattering in terms of the polar and azimuthal scattering angles θ and ϕ.

(3) The change in position.

(4) The energy loss due to inelastic scattering.

In addition, in the presence of interfaces between different materials and/or scoring regions, a boundary crossing algorithm is required. The interface problem is illustrated in Fig. 1. The transport between points A and B is simulated by the dashed straight line. As indicated in the figure, some of the curved real trajectories, starting at A and ending at B, may pass through region 2. If the media in the regions 1 and 2 are identical, a simulation as shown in the figure may lead to an incorrect energy deposition calculation in the two regions. If, on the other hand, the two media are different, the simulation of the transport in the vicinity of the interface will affect the entire particle history. The interface problem was already pointed out in Ref. 7.

In this report the attention is focused on a class II CH implementation, although some of the results are also applicable to class I schemes. The multiple elastic scattering theory implemented in EGSnrc will be discussed in Sec. II A. The algorithm determining the position change is given in Sec. II B. The calculation of the energy loss associated with a given step length is presented in Sec. II D. Sampling distances between subsequent discrete interactions is discussed in Sec. II C. Although, in principle, these distances could be the only factor determining CH step lengths, additional step-size restrictions are required to assure the accuracy of the algorithms involved, as it will become clear from Sec. II A–II D. The EGSnrc boundary crossing algorithm is discussed in Sec. II E. Finally, some technical details of the implementation are given in Sec. II F.

A. Multiple scattering

The use of Molière's multiple scattering (MS) theory has been considered in the past as one of the main disadvantages of EGS4 compared to class I algorithms, where the exact Goudsmit–Saunderson (GS) formulation[8,9] with the latest partial-wave analysis (PWA) cross sections (see, e.g., Ref. 10) can be used. In a recent paper Kawrakow and Bielajew have shown that the use of the GS theory is possible in a class II algorithm.[11] The MS theory, which is based on the screened Rutherford single elastic scattering cross section, presented in Ref. 11, is implemented in EGSnrc. The implementation of a MS theory based on PWA cross sections[12] is left for future development of the system. Here, we will discuss a slight improvement of energy loss considerations as compared to the approach presented in Ref. 11.

The moments κ_l of the elastic scattering cross section $\sigma(\chi,E)$,

$$\kappa_l(E)=2\pi N\int_{-1}^{1}\mathrm{d}\cos\chi\,\sigma(\chi,E)[1-P_l(\cos\chi)], \tag{1}$$

play a central role in the MS theory of Goudsmit and Saunderson,[8,9] as well as in the theory of Lewis.[13] Here, the P_l's are Legendre polynomials, E is the kinetic energy of the particle, and N is the density of scattering centers (atoms or molecules). The GS multiple scattering distribution for a pathlength s, corresponding to an energy loss ΔE, is

$$F_{\mathrm{GS}}(\cos\theta)=\sum_{l=0}^{\infty}(l+1/2)k_lP_l(\cos\theta), \tag{2}$$

where

$$k_l=\exp(-G_l),\quad G_l=\int_0^s \mathrm{d}s'\,\kappa_l[E(s')]$$
$$=\int_{E_i-\Delta E}^{E_i}\frac{dE}{L(E)}\kappa_l(E), \tag{3}$$

E_i being the initial kinetic energy and $L(E)$ the restricted or unrestricted stopping power (restricted stopping power is to be used if the simulation is performed with secondary particle production taken into account). The MS theory of Ref. 11 was developed by initially neglecting energy loss (i.e., $G_l=\kappa_l s$). Energy loss was then taken into account by applying approximate corrections to the G_l's, which allow for the use of the no-energy loss distribution. An improvement compared to this approach is presented in Appendix A and demonstrated in Fig. 2. This figure shows the ratio of the multiple scattering distribution calculated with the approach presented in Appendix A [G_l given by Eqs. (A3), (A6)] and the MS distribution calculated according to the approach of Ref. 11 [G_l given by Eq. (A1)] to the exact MS distributions with G_l's obtained from a 64-point Gauss–Legendre integration of Eq. (3) for 10 MeV and 100 keV electrons in graphite and a pathlength corresponding to 25% energy loss. The qualitative behavior for other materials is similar. Note that a step length corresponding to 25% energy loss was selected in order to demonstrate the maximum error to be expected

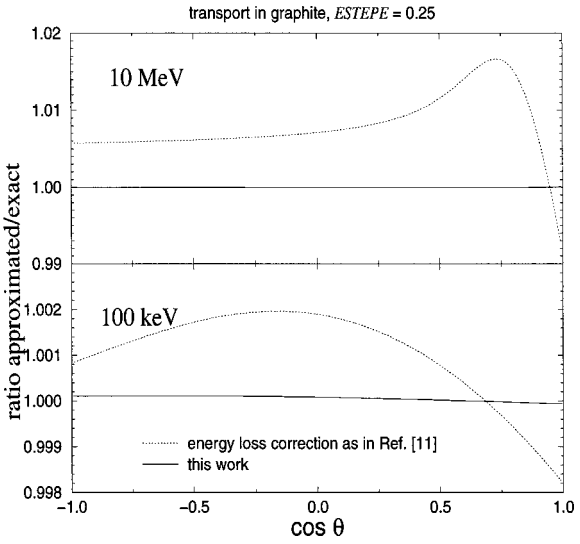

FIG. 2. The ratio of the multiple scattering distribution calculated with two different approximations for the moments G_l to the exact MS distribution obtained by a 64-point Gauss–Legendre quadrature of Eq. (3) for 10 MeV and 100 keV electrons in graphite and a pathlength corresponding to 25% energy loss. The solid line corresponds to the improved approach discussed in Appendix A; the dashed line to the approach presented in Ref. 11.

without the energy loss corrections-discussed here (25% is the maximum energy loss per step recommended in EGSnrc; see Sec. II D).

B. Electron-step algorithm

Due to multiple scattering, electrons do not move on straight lines during a CH step. The difference between the curved electron trajectory length, s, and the transport distance in the original direction of motion, $\langle z\rangle$, has become known as a pathlength correction (PLC). The deflection from the line along the initial direction of motion is referred to as lateral deflection or lateral correlation. The algorithm used to account for these effects will be referred to as the electron-step algorithm.

In the original EGS4 version,[3] lateral deflections are neglected and PLCs are modeled according to Fermi–Eyges theory.[14] In PRESTA,[15] the final position of the electron is calculated according to

$$x=\frac{s}{2}\sin\theta\cos\phi,$$
$$y=\frac{s}{2}\sin\theta\sin\phi, \tag{4}$$
$$z=\langle z\rangle,$$

where θ and ϕ are the polar and azimuthal scattering angles at the end of the step and the process is considered in a frame with the origin coinciding with the initial position and z direction along the initial direction of motion.

Apart from the lack of longitudinal straggling, it was shown in Ref. 16 that this algorithm underestimates the average lateral deflection and also produces an unphysical singularity in the lateral deflection distribution. A detailed discussion of PRESTA and other electron-step algorithms is given in Ref. 17. In this paper a new electron-step algorithm was constructed in such a way as to reproduce first- and second-order spatial moments (e.g., $\langle z\rangle$, $\langle z^2\rangle$, $\langle r^2\rangle$, $\langle z\cos\theta\rangle$, etc.), which are known from the theory of Lewis.[13] According to this algorithm, the final position of the electron is calculated from

$$\begin{aligned}
x&=s[\,\eta\delta\sin\theta_1\cos\phi_1+\eta(1-\delta)\sin\theta_2(\cos\phi_1\cos\phi_2\\
&\quad-\cos\theta_1\sin\phi_1\sin\phi_2)+a_2\sin\theta\cos\phi],\\
y&=s[\,\eta\delta\sin\theta_1\sin\phi_1+\eta(1-\delta)\sin\theta_2(\sin\phi_1\cos\phi_2\\
&\quad+\cos\theta_1\cos\phi_1\sin\phi_2)+a_2\sin\theta\sin\phi],\\
z&=s[a_1+\eta\delta\cos\theta_1+\eta(1-\delta)\cos\theta_2+a_2\cos\theta]\\
a_1&=a_2=\frac{1-\eta}{2}.
\end{aligned} \tag{5}$$

Here, η is a random number sampled from $2\eta\,\mathrm{d}\eta$, θ_1, ϕ_1 and θ_2, ϕ_2 polar and azimuthal scattering angles for the first and second substep. Note that the actual condensed history step is divided into two substeps with their own multiple scattering angles. This approach was motivated by the fact that no order of magnitude improvement of the truncation error can be achieved with a single MS angle per CH step (see Refs. 17 and 18). The final scattering angle is calculated from θ_1, and ϕ_1 and θ_2, ϕ_2, e.g. $\cos\theta=\cos\theta_1\cos\theta_2-\sin\theta_1\sin\theta_2\cos(\phi_1-\phi_2)$. The parameter δ is given by

$$\delta=\frac{1}{2}+\frac{\sqrt{6}}{6}-\left(\frac{1}{4\sqrt{6}}-\gamma\frac{4-\sqrt{6}}{24\sqrt{6}}\right)\xi\mp\cdots. \tag{6}$$

Here and in what follows we frequently make use of the first two elastic scattering moments G_1 and G_2 [see Eq. (3)] and give them therefore special names,

$$\xi=G_1,\quad \gamma=G_2/G_1. \tag{7}$$

Note that the parameters a_1, a_2, and δ of the electron-step algorithm given by Eq. (5) were obtained previously neglecting energy loss during the step. This approach allowed for power series expansions of the moments, known from the theory of Lewis, in terms of ξ, which simplified the analysis significantly and made the construction of the new algorithm easier. For realistic simulations, corrections to the parameters a_1, a_2, and δ are necessary in order to properly take into account energy loss during the step. The derivation of these corrections is presented in Appendix B. Their effect on the simulated ion chamber cavity dose is discussed in Sec. III D in paper II.

In Fig. 3 (lower part) the ratio of the spatial moments $s-\langle z\rangle$, $\langle r^2\rangle$, $s-\langle z\cos\theta\rangle$ and $\langle x\sin\theta\cos\phi\rangle$, calculated including the energy loss corrections of Appendix B, to the corresponding exact moments is shown as a function of energy for the maximum step length (see Sec. II F) in graphite. A similar behavior is observed in other materials. The very good agreement was the main motivation to restrict the correction of the parameters a_1, a_2 and δ to $O(\Delta E)$. To demonstrate the improvement compared to Ref. 17, the same

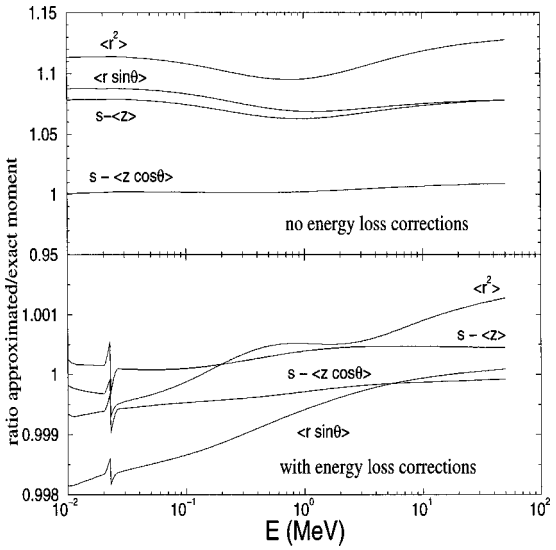

FIG. 3. The ratio of various moments resulting from the electron-step algorithm of Ref. 17 to the exact moments from the theory of Lewis. Values are calculated for graphite using the largest step size allowed (25% energy loss). The lower portion shows results when energy loss corrections according to Appendix B, Eqs. (B5)–(B7), are taken into account. The upper portion of the figure shows the same moments calculated without these corrections.

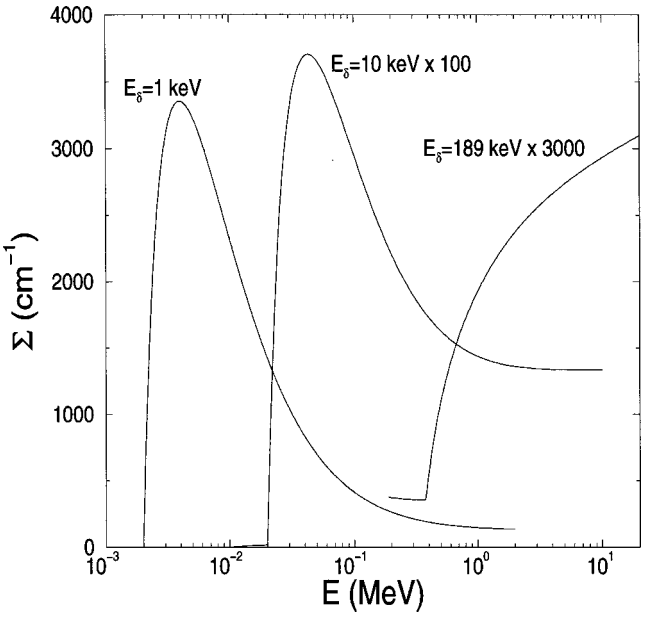

FIG. 4. The total cross section for discrete interactions in graphite, calculated with $E_\gamma = E_\delta = 1$ keV, $E_\gamma = E_\delta = 10$ keV (scaled by a factor of 100), and $E_\gamma = 10$ keV, $E_\delta = 189$ keV (scaled by a factor of 3000), as a function of kinetic energy.

ratio calculated without the energy loss corrections, is shown in the upper part of this figure. Note that the discontinuity around 20 keV is caused by the use of stopping power derivatives that are discontinuous around the delta particle production threshold energy (20 keV in this case).

C. Discrete interactions

The unnormalized conditional probability that a discrete interaction occurs after a pathlength s is

$$P(s) = \exp\left(-\int_0^s ds' \, \Sigma(s') \right), \tag{8}$$

where $\Sigma(s)$ is the total macroscopic particle production cross section above the specified threshold energies E_γ and E_δ. Sampling transport distances between discrete interactions on the basis of (8) can be accomplished by solving the equation

$$\int_0^s ds' \, \Sigma(s') = \lambda = -\ln \eta, \tag{9}$$

where λ is the number of mean-free paths and η is a uniformly distributed random number between zero and unity. When Σ is independent of s (e.g., in the case of photon transport), the above equation simplifies to the familiar expression

$$s = -\ln \eta / \Sigma. \tag{10}$$

To avoid a numerically intensive solution of Eq. (9) the so-called fictitious cross section method is employed in EGS4 to sample distances between discrete interactions:[3] a fictitious process, the result of which is to leave energy and direction of the particle unchanged, is added to the list of interactions. The cross section for this process, Σ_f, is chosen in such a way that

$$\Sigma(s) + \Sigma_f(s) = \Sigma_0 \equiv \text{const.} \tag{11}$$

Equation (10) with $\Sigma = \Sigma_0$ can then be used to sample s. Once s is determined and the particle transported to the interaction site, the interaction is rejected with the probability $1 - \Sigma(s)/\Sigma_0$ (or, equivalently, a fictitious interaction takes place with the probability $1 - \Sigma(s)/\Sigma_0$). A proof that the fictitious cross section method correctly reproduces the number of discrete interactions, provided $\Sigma_0 \geqslant \Sigma(s)$ for all s, is given in Appendix C. EGS4, being initially developed for high-energy applications, uses $\Sigma_0 = \Sigma(E_i)$, where E_i is the energy at the beginning of the step. This is motivated by the fact that at high energies the electron cross section for discrete processes decreases with decreasing energy. For energies of the order of a few hundred keV and a sufficiently low threshold energy E_δ, however, the cross section starts to increase with decreasing energy until it reaches a maximum around $4E_\delta$. This can be seen in Fig. 4, where the total discrete interaction cross section in graphite is shown as a function of energy for $E_\gamma = E_\delta = 1$ keV, $E_\gamma = E_\delta = 10$ keV and $E_\gamma = 10$ keV, $E_\delta = 189$ keV. The qualitative behavior of the cross section is similar in other materials. This fact, pointed out already in Ref. 19, leads to the breakdown of the fictitious cross section method and an associated underprediction of energy loss due to discrete interactions. Taking into account only the leading energy dependence of the delta particle production cross section, $\Sigma_\delta(E)$, it is easy to show that $\Sigma_\delta(E)$ has a maximum at $E_{\max}$,

$$E_{\max}=\frac{m}{2E_\delta}(m-3E_\delta+\sqrt{(m+E_\delta)(m-7E_\delta)})$$
$$\approx 4E_\delta\left(1+3\frac{E_\delta}{m}\pm\cdots\right), \quad (12)$$

if $E_\delta<m/7$, m being the electron's rest energy. Otherwise $\Sigma_\delta(E)$ is a monotonically increasing function of energy.

A cutoff energy of 10 keV or less is frequently employed for the simulation of detector response. Also, the energy region below 1 MeV is of particular importance for the dose deposited in the sensitive volume of an ion chamber and so, Ma and Nahum have proposed a modification of the fictitious cross section method for use with EGS4.[20] Unfortunately, it turns out that their method is biased, as shown in Appendix C.

The fictitious cross section method can be applied in any situation if $\Sigma_0=\Sigma_{\max}$ is used to sample distances between subsequent interactions. The efficiency of such an approach rapidly decreases with decreasing cutoff energy E_δ. For instance, for $E_\delta=1$ keV (kinetic energy), only in one out of 22 cases will a real interaction take place for a 1 MeV electron in graphite (see Fig. 4). In this paper we will present a simple method for sampling distances between discrete interactions that does not become very inefficient for low E_δ. The distance between discrete interactions can be measured with variables other than the pathlength. If we use the energy loss to subthreshold processes to determine the occurrence of discrete collisions, we have, for the conditional probability, that a collision occurs after an energy loss ΔE,

$$P(\Delta E)=\exp\left(-\int_{E_i-\Delta E}^{E_i}\mathrm{d}E\,\Sigma_E(E)\right), \quad (13)$$

where E_i is the kinetic energy at the beginning of the step and Σ_E the interaction cross section per unit energy loss.

$$\Sigma_E(E)=\frac{\Sigma(E)}{L(E,E_\gamma,E_\delta)}, \quad (14)$$

$L(E,E_\gamma,E_\delta)$ being the restricted stopping power. The quantity $\Sigma_E(E)$, calculated with $E_\gamma=E_\delta=1$ keV and $E_\gamma=E_\delta=10$ keV, is shown in Fig. 5 for graphite and gold. We see from this figure that the variation with energy is strongly reduced compared to $\Sigma(E)$ and that, for a given material, there is a single maximum $\Sigma_{\mathrm{E}}^{\max}$ that can be used for the fictitious cross section method. Most of the interactions will be real, except at energies approaching E_δ. For such low energies, however, the maximum fractional energy loss per step (ESTEPE) will usually be a stronger step-size restriction than the distance between subsequent discrete interactions. In graphite, for instance, the average energy loss between discrete interactions will be ~160 keV, which is of the same order as the energy where Σ_E starts to decrease with decreasing energy. Note also that the use of $\Sigma_{\mathrm{E}}^{\max}$ to sample distances between discrete interactions avoids the necessity to evaluate the cross section at the beginning of every TSTEP loop, as in the current EGS4 implementation.

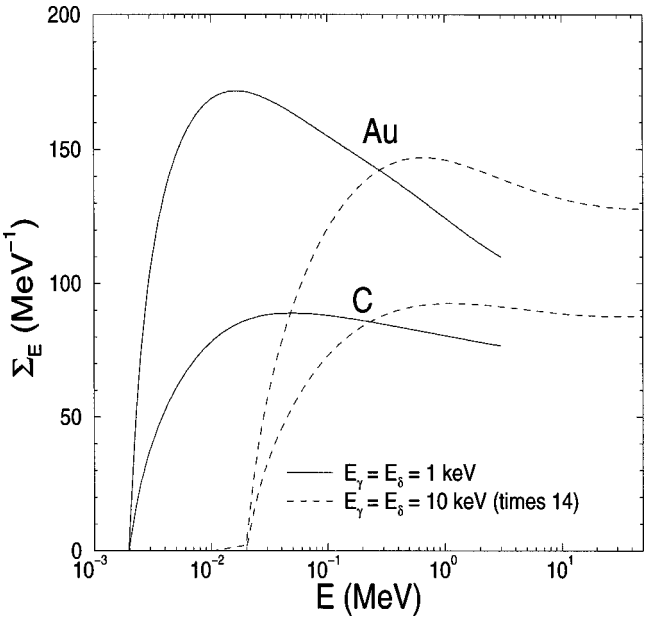

FIG. 5. The total cross section per unit energy loss, Σ_E, for discrete interactions in graphite and gold, calculated with $E_\gamma=E_\delta=1$ keV and $E_\gamma=E_\delta=10$ keV (scaled with a factor of 14 for better visibility) as a function of kinetic energy.

Once the energy loss to the next discrete interaction is sampled, the corresponding pathlength has to be calculated according to

$$s=\int_{E_i-\Delta E}^{E_i}\frac{\mathrm{d}E}{L(E)} \quad (15)$$

(for the sake of brevity we omit here and in the following discussions the threshold energy dependence of the restricted stopping power). The evaluation of this and other integrals involving energy-dependent quantities will be discussed in the next section.

D. Energy loss

The CH simulation of electron transport requires the evaluation of integrals involving energy-dependent quantities. The evaluation of multiple scattering related integrals was discussed in Sec. II B and Appendix B. In this section we will consider energy loss integrals. We will frequently make use of the formula

$$\int_{x-\Delta x/2}^{x+\Delta x/2}\mathrm{d}x'\,f(x')=f(x)\Delta x+f''(x)\frac{\Delta x^3}{24}+O(\Delta x^5), \quad (16)$$

where f is any two times differentiable function and f'' its second-order derivative with respect to x.

The first example of an energy loss integral is Eq. (15). A direct application of (16) yields

$$s=\frac{\Delta E}{L(\tilde{E})}\left(1+\frac{2L'(\tilde{E})^2-L(\tilde{E})L''(\tilde{E})}{L(\tilde{E})^2}\frac{\Delta E^2}{24}+O(\Delta E^4)\right), \quad (17)$$

with L' and L'' denoting the first- and second-order derivatives of the (restricted) stopping power L with respect to E and $\tilde{E}=E_i-\Delta E/2$ the average energy. Here and in what follows we will use $L(E)$ to denote both the restricted and unrestricted stopping power, depending on whether a CSDA or full calculations are discussed. This choice was made because in many cases the formulas are applicable to both cases. Strictly speaking, the above equation is not applicable in the vicinity of the δ particle and bremsstrahlung production threshold energies, $2E_\delta$ and E_γ, because L' has discontinuities at $E=2E_\delta$ and $E=E_\gamma$, and so L'' does not exist for these energies. In order to avoid this difficulty and to save the evaluation of L'', we make use of the approximation

$$\frac{E^2}{C(E)^2}\frac{\mathrm{d}^2C(E)}{\mathrm{d}E^2}\approx -b(E), \tag{18}$$

where $C(E)$ and $b(E)$ are defined in Eq. (A7). The above equation is valid for energies not too close to the mean ionization potential I and results from the (restricted) stopping power formula with neglect of terms small compared to $\ln E/I$. With this approximation, Eq. (17) becomes

$$s\approx\frac{\Delta E}{L(\tilde{E})}g(\tilde{\tau},\epsilon), \tag{19}$$

$$g(\tilde{E},\epsilon)=1+\frac{2b^2(1+\tilde{\tau})^2(2+\tilde{\tau})+b(1+\tilde{\tau})(\tilde{\tau}^2+3\tilde{\tau}-2)-6\tilde{\tau}}{6(1+\tilde{\tau})^2(2+\tilde{\tau})}\times\left(\frac{\epsilon}{2-\epsilon}\right)^2+O(\epsilon^4),$$

where $\tilde{\tau}=\tilde{E}/m$, $\epsilon=\Delta E/E_i$, and $b=b(\tilde{E})$. Figure 6 shows the ratio of s, calculated according to Eq. (19), to the exact pathlength, calculated by numerical integration of (15), for $\epsilon=0.25$ and $E_\delta=10\,\mathrm{keV}$ in graphite, aluminum, and gold. We see that the agreement is of the order of 0.01%, except in the vicinity of the delta particle production threshold. The correction $g(\tilde{E},\epsilon=0.25)$ is of the order of 3%–4% at low energies and high-Z materials and is negligible for energies above a few MeV. Note that Eq. (19) has an $O(\epsilon^4)$ error so that the deviation from the exact result is much smaller for smaller ϵ. On the other hand, the error rapidly increases for larger fractional energy losses per step, therefore the restriction $\epsilon\leqslant 0.25$ is recommended for subpercent accuracy.

The actual electron step length in a CH simulation will be frequently shorter than the pathlength between discrete interactions due to user defined step-size restrictions, geometry constraints, etc. In such situations, the subthreshold processes energy loss must be calculated according to

$$\Delta E=\int_0^s \mathrm{d}s'\,L(E(s')). \tag{20}$$

In standard EGS4, the above integral is approximated by

$$\Delta E\approx L(E_i)s\equiv\Delta E_1. \tag{21}$$

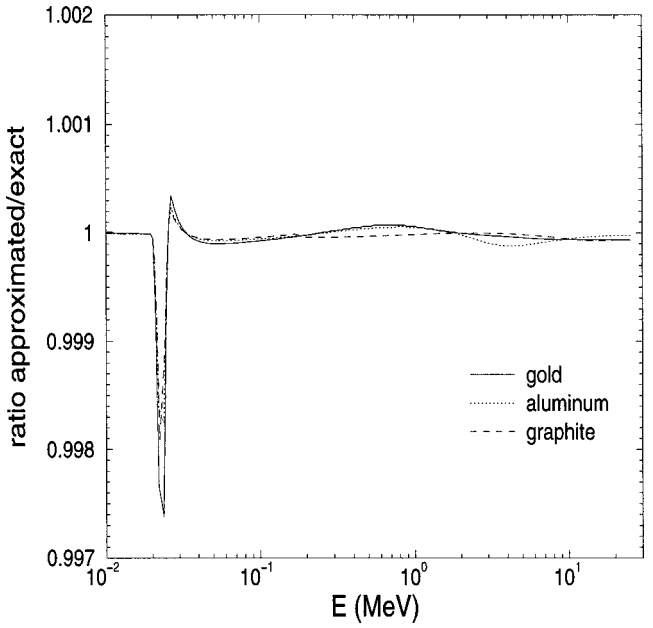

FIG. 6. The ratio of the exact pathlength between discrete interactions, calculated by numerical integration of Eq. (15), to the approximated pathlength calculated according to Eq. (19) in gold (solid line), aluminum (dotted line), and graphite (dashed line) as a function of kinetic energy for $\epsilon=0.25$ and $E_\gamma=E_\delta=10$ keV.

This approximation is motivated by the fact that at high energies the (restricted) stopping power varies very slowly with energy. In PRESTA, the energy loss is estimated by

$$\Delta E\approx L(E_i-\Delta E_1/2)s. \tag{22}$$

This treatment is motivated by Euler's integration formula [see Eq. (16)] and the resulting expectation for a $O(\epsilon^2)$ error (ϵ is the energy loss fraction associated with a pathlength s; see Ref. 15). A simple calculation reveals, however, that in the case of the integral (20), the use of Eq. (22) leads to an $O(\epsilon)$ error [simply because ΔE_1 has an $O(\epsilon)$ error]. Although an improvement compared to (21), PRESTA's approximation is not accurate enough for low-energy electron transport if one is interested in a dose calculation with subpercent accuracy. A more accurate evaluation of the integral in Eq. (20) is given in Appendix D.

The ratio of the energy loss, calculated according to Eq. (D.4) from Appendix D, to the exact energy loss for a pathlength corresponding to $\epsilon=0.25$ in graphite is shown in Fig. 7. As in the previous figures, the behavior for other materials is similar. For comparison, PRESTA's approach as well as the result of Eq. (D.2) for ΔE_2 (the first-order approximation to ΔE derived in Appendix D) is also included in this figure. Note that if we were not interested in a very high accuracy, it would suffice to use ΔE_2 as an estimate of the energy loss. This would save the reevaluation of the midpoint stopping power and the associated calculation of a logarithm (logarithmic interpolation is used in EGS4 to calculate energy-dependent quantities).

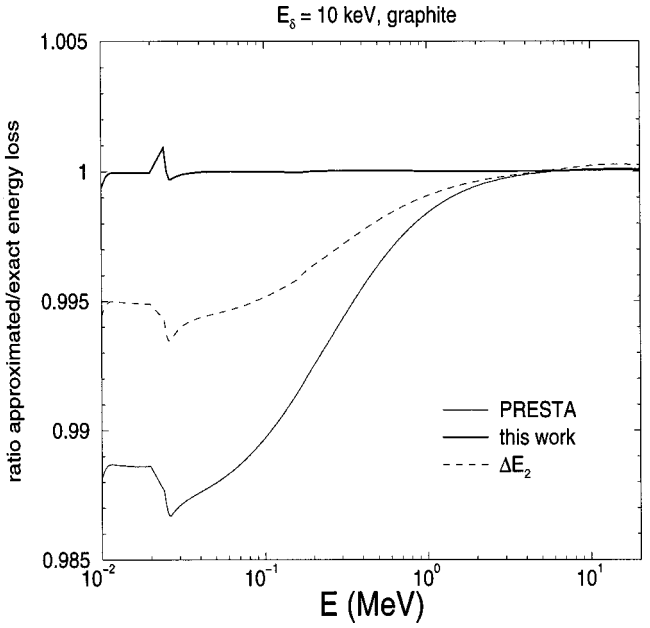

FIG. 7. The ratio of the subthreshold processes energy loss for a pathlength corresponding to $\epsilon=0.25$ calculated with various approaches to the exact energy loss obtained by numerical integration of Eq. (20). Thin solid line: PRESTA (midpoint energy evaluation); dashed line: this work, Eq. (D2); thick solid line: this work, Eq. (D4).

E. Boundary crossing algorithm

To address the so-called interface artifact mentioned in the beginning of Sec. II, a refined boundary crossing algorithm (BCA) was incorporated in PRESTA. According to this algorithm, the electron is not allowed to take a step longer than $t_\perp$, $t_\perp$ being the perpendicular distance to the closest boundary, unless $t_\perp$ becomes smaller than $t_{\min}$, a user defined minimum step length for boundary crossing. For $t_\perp < t_{\min}$, lateral deflections are switched off and the particle is transported, as in the case of standard EGS4, on a straight line to the boundary.

In a more recent paper,[21] Foote and Smyth have demonstrated that the approach of forcing a multiple scattering event at the boundary causes a singularity in the simulated particle fluence. The singularity results from the fact that there is a nonzero probability for scattering parallel to the boundary. Note that in real life, particles moving parallel to the boundary do not cross it and therefore do not contribute to the planar fluence. Although the singularity is present in any situation over a distance of the order of $t_{\min}$, it will be observed, e.g., as a dose overprediction, only if the size of a scoring region is comparable to $t_{\min}$ due to averaging. An immediate example of a situation where standard EGS4's and PRESTA's BCA should produce a dose surplus is the cavity of an ion chamber or a thin air slab, as discussed in Ref. 22.

To overcome this difficulty, PRESTA's boundary crossing algorithm has been modified to switch to single scattering simulation of elastic scattering whenever a particle comes closer to a boundary than $t_{\min}$. Whereas in the case of PRESTA one of the criteria to determine $t_{\min}$ was to assure the applicability of Molière's MS theory, here the only criterion for $t_{\min}$ is efficiency. It turns out that single scattering simulation becomes more efficient than CH at about three elastic mean-free paths (MFP). This is taken as a default, although the user can determine $t_{\min}$ by setting the appropriate parameter (see next section).

Sampling distances between subsequent elastic collisions could be done by an appropriate version of the fictitious cross section method (see Sec. II C). However, due to the fact that the elastic scattering cross section Σ_e is very large (and therefore energy loss between subsequent elastic collisions very small), it is possible to use Eq. (9) directly. To do so, we use a Taylor expansion of Σ_e around the initial energy E_i to arrive at

$$\int_0^s ds'\,\Sigma_e(s') \approx \Sigma_e(E_i)s - L(E_i)\Sigma_e'(E_i)\frac{s^2}{2} + L(E_i)^2\left(\frac{L'(E_i)}{L(E_i)}\Sigma_e'(E_i)+\Sigma_e''(E_i)\right)\frac{s^3}{6}, \tag{23}$$

for the left-hand side of Eq. (9). Here, Σ_e' and Σ_e'' are first- and second-order derivatives of Σ_e with respect to E. With this result, the pathlength s corresponding to λ MFPs is

$$s \approx \frac{\lambda}{\Sigma_e(E_i)}\left\{1+\frac{E_i\Sigma_e'(E_i)}{\Sigma(E_i)}\frac{\epsilon}{2}+\left[3\left(\frac{E_i\Sigma_e(E_i)}{\Sigma_e(E_i)}\right)^2 - \frac{E_iL'(E_i)}{L(E_i)}\frac{E_i\Sigma_e(E_i)}{\Sigma_e(E_i)} - \frac{E_i^2\Sigma_e''(E_i)}{\Sigma_e(E_i)}\right]\frac{\epsilon^2}{6}\right\}, \tag{24}$$

where $\epsilon=\lambda L(E_i)/(\Sigma_e(E_i)E_i)$ is the energy loss fraction for the pathlength resulting from a constant cross section $\Sigma_e(E_i)$ and usually a very small quantity. Presently, the total elastic cross section used in EGS4 is $\Sigma_e=b_c/\beta^2$, which gives

$$s \approx \frac{\lambda\beta_i^2}{b_c}\left\{1-\frac{\epsilon}{(\tau_i+1)(\tau_i+2)} + \frac{\epsilon^2}{(\tau_i+1)^2(\tau_i+2)}\left[\frac{b(E_i)}{3}(\tau_i+2)-\tau_i\right]\right\}. \tag{25}$$

Here, τ_i again denotes the ratio of the initial energy E_i to the electron's rest energy m and $b(E_i)$ is the quantity defined in Eq. (A7). The ratio of the pathlength corresponding to 15 MFPs (the probability to sample $\lambda \geqslant 15$ is 3×10^{-7}!), calculated from Eq. (25), to the pathlength found by the numerical solution of Eq. (9) as a function of energy is shown in Fig. 8. The material was graphite and the unrestricted stopping power was used. To demonstrate that the corrections discussed above are really required, the result of the zeroth-order approximation [i.e., $s=\lambda/\Sigma_e(E_i)$, dotted line] and the first-order result (thin full line) are also shown. For energies above 10 keV the use of the first-order result is sufficiently accurate. Note also that the use of the second-order expression requires only minor additional calculation as $b(E)$ is already calculated for the energy loss evaluation at the time single scattering sampling occurs.

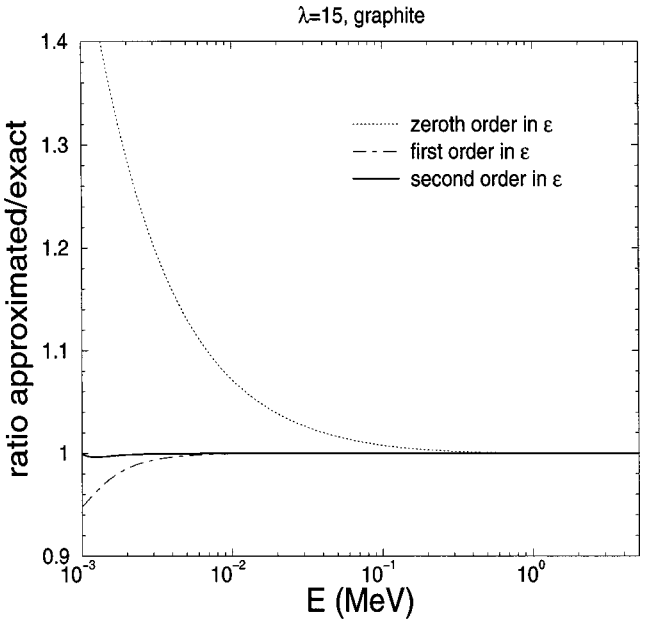

FIG. 8. The ratio of the pathlength between subsequent elastic collisions for $\lambda=15$ MFP, calculated to zeroth (dashed line), first (dot–dashed line), or second (solid line) order in ϵ, to the exact pathlength (see the text).

F. Implementation

To implement the new multiple scattering theory, the new electron-step algorithm and other modifications discussed in the previous sections, a complete recoding of the EGS4 electron transport routine ELECTR was necessary. However, to assure compatibility with existing EGS4 user codes, the general logic of the code was retained, accepting in some cases a slight loss in efficiency. Also for compatibility reasons, and in order to make possible the evaluation of the effect of various transport options on the calculated results, the user can choose between exact boundary crossing (see the last section) or PRESTA's BCA, and between the electron-step algorithm discussed in Sec. II B or a slightly modified version of PRESTA's transport algorithm. This modified version uses PRESTA's LCA, but the exact expression for $\langle z \rangle$ given by Lewis [see Eqs. (B1)–(B3)], which is faster to calculate and more accurate than the original PRESTA formula for the pathlength correction derived from the theory of Molière. In addition, the minimum step size for boundary crossing, $t_{\min}$, can be controlled by the user so that even standard EGS4 behavior can be recovered by choosing PRESTA's BCA and $t_{\min} \rightarrow \infty$. Various possible electron transport modes that result from different settings of the transport parameters are summarized in Table I.

In addition to the ESTEPE parameter, which controls the maximum fractional energy loss per step, there is now another step-size constraint that restricts a CH step to a given maximum first MS moment, i.e., $\xi \leqslant \xi_{\max}$. As discussed in Ref. 17, the truncation error of the new electron-step algorithm for first- and second-order spatial moments is below 0.1% for $\xi \leqslant 0.5$. Note that a similar step-size restriction was already present, but not accessible for the user, in the original EGS4 version due to the requirement that the average multiple scattering angle in a CH step is not larger than a radian [see Eq. (2.14.74) in Ref. 3]. Note that the average multiple scattering angle squared is roughly given by 2ξ so that the original EGS4 constraint also corresponds to $\xi \leqslant 0.5$. Figure 9 shows the maximum fractional energy loss per step in graphite and aluminum as a function of energy for ESTEPE=0.25 and $\xi_{\max}=0.5$. We see that at low energies, the $\xi_{\max}$ constraint, introduced to guarantee the accuracy of the MS algorithm, is more restrictive. At high energies, the ESTEPE constraint, necessary to assure accurate energy loss evaluation and correct sampling of distances between discrete interactions, determines the maximum step size.

It is beyond the purpose of this report to give a detailed discussion of the ''cost'' of the improvements discussed here

TABLE I. Summary of the electron transport algorithms possible with EGSnrc. The last column gives the algorithm resulting from the choice of the parameters in columns 1–3. The new ELECTR routine switches to single elastic scattering (if exact_bca=true) or turns off lateral deflection (if exact_bca=false) at a perpendicular distance skindepth_for_bca from a boundary (measured in elastic mean-free paths; for a definition of $b_{\min}$ see Ref. 15). Lateral deflections and pathlength corrections in ''normal'' condensed history transport (away from boundaries) are modeled according to the algorithm presented in Ref. 17 and improved in Appendix B (if transport_algorithm=0) or according to the PRESTA algorithm (if transport_algorithm=1). The choice of transport_algorithm is irrelevant if skindepth_for_bca is set to infinity and exact_bca=true, as the entire simulation is then performed in a single scattering mode.

exact_bca	transport_algorithm	skindepth_for_bca	Electron transport
True	0	3	Exact boundary crossing, improved LCA and PLCs ≡EGSnrc default settings
True	0 or 1	∞	Single scattering simulation in the entire geometry
True	1	e.g., $\exp(b_{\min})$	PRESTA CH transport but exact boundary crossing
False	0	e.g., $\exp(b_{\min})$	Behaves like PRESTA in the vicinity of boundaries but improved LCA and PLC
False	1	$\exp(b_{\min})$	PRESTA
False	1	∞	Standard EGS4

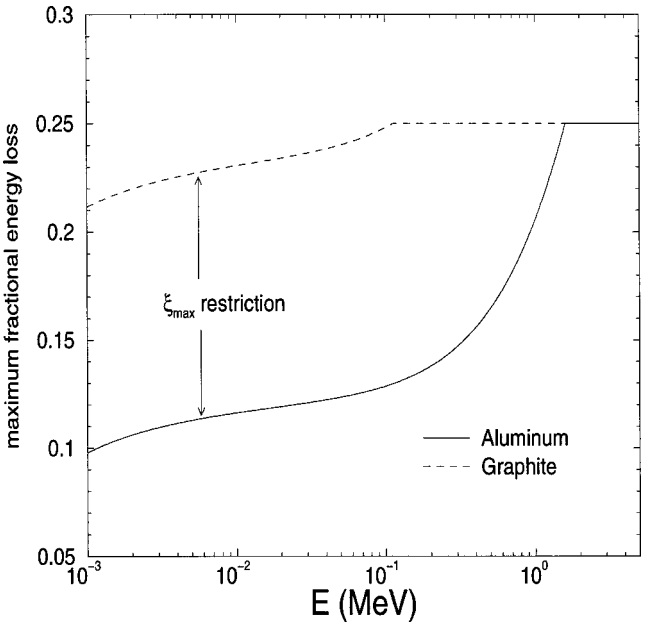

FIG. 9. The maximum fractional energy loss per step resulting from ESTEPE=0.25 and $\xi_{max}=0.5$ in aluminum and graphite as a function of kinetic energy.

in terms of calculation speed. Extensive benchmark comparisons between EGSnrc and EGS4/PRESTA will be part of the official release of the system and will provide more insight into this issue. Nevertheless, the following general observations can be made at this time.

(1) As EGSnrc's electron-step algorithm has a truncation error that is smaller than that of EGS4/PRESTA by an order of magnitude,[17] it is clear that the new code is more efficient in situations with only few boundaries.

(2) In situations with many boundaries EGS4/PRESTA is likely to be faster. There are, however, no general rules for the *precise* amount of CPU time increase, this increase being dependent on the geometrical size of the regions, the EGS4/PRESTA minimum step size for boundary crossing, energy, cutoffs, etc.

(3) In the ''intermediate'' case, the speed will depend on the balance between long condensed history steps and single scattering simulation in the vicinity of boundaries.

As an example for a situation with many boundaries, a typical calculation for radiation treatment planning requires three times more CPU time with EGSnrc than with EGS4/PRESTA. Note, however, that for this type of calculation, where the accuracy of EGS4/PRESTA has been established in the past, the user can ''turn on'' PRESTA within EGSnrc. In this case EGSnrc was found to be typically about 5% faster than EGS4/PRESTA because of the faster MS routine and pathlength-correction calculation. For the two examples discussed in the next section, EGSnrc is substantially more efficient than EGS4/PRESTA. In the case of ion chamber simulations EGSnrc with default step sizes is about five times faster than EGS4/PRESTA with ESTEPE of 1%, which is recommended and necessary for this type of calculation.[23] The gain in calculation speed is even more dramatic for the backscattering calculations, where the correct result can be obtained in less than one-tenth the CPU time. Finally, it is worth noticing that having confidence in the accuracy of the calculated results without potentially time consuming step-size dependence studies may be of great value in a variety of situations.

III. EXAMPLES

In this section results of EGSnrc ion chamber and backscattering simulations, situations that have been considered in the past as two of the most stringent tests of CH Monte Carlo codes, are briefly presented. A detailed discussion of the effect due to the inaccurate implementation of the various CH components on the simulated cavity dose is given in the accompanying paper.

A. Ion chamber simulation

In the first example, a pancake graphite or aluminum ionization chamber with full buildup wall thickness was irradiated with a 1.25 MeV parallel photon beam incident on the flat side. At this energy, being the average energy of a 60 Co beam, artifacts due to the inaccurate CH implementation are maximized or close to maximized. This fact can be understood if one takes into account that at low photon energies electron transport plays no role and at high energies electron elastic scattering and also energy dependence in stopping powers is much weaker. In order to be able to test the accuracy of the MC simulation rigorously, the chamber cavity was filled with wall material with a much lower density (the density effect correction on the collision stopping power was calculated, however, using the wall density). For this situation, the dose to the cavity per incident energy fluence, after correction for wall attenuation and scatter, is simply given by the mass energy-absorption coefficient of the wall material (see paper II for details).

The ratio of the simulated cavity dose to the theoretically known answer is shown in Fig. 10. This figure demonstrates that the calculated ion chamber response is independent of step size and agrees with the known answer to within 0.1% (the statistical uncertainty on the simulated cavity dose was 0.05%). For comparison, the EGS4/PRESTA step-size variation for a similar situation, reported in Ref. 23, is 2.5% for graphite walled chambers and over 5% for aluminum chambers.

B. Backscattering

As a second example, the energy fraction reflected on a semi-infinite water surface for perpendicularly incident electron beams of various energies was calculated as a function of step size using EGSnrc. For this situation, reported EGS4/PRESTA calculations show step-size variations of up to 100%.[15]

Figure 11 shows results for 0.01, 0.1, 1, and 10 MeV. All calculations are normalized to the results of single elastic scattering simulations at the corresponding energies. The 10 MeV calculations were performed without the production of secondary particles (full simulation with secondary particle creation required too long a calculation time in a single scat-

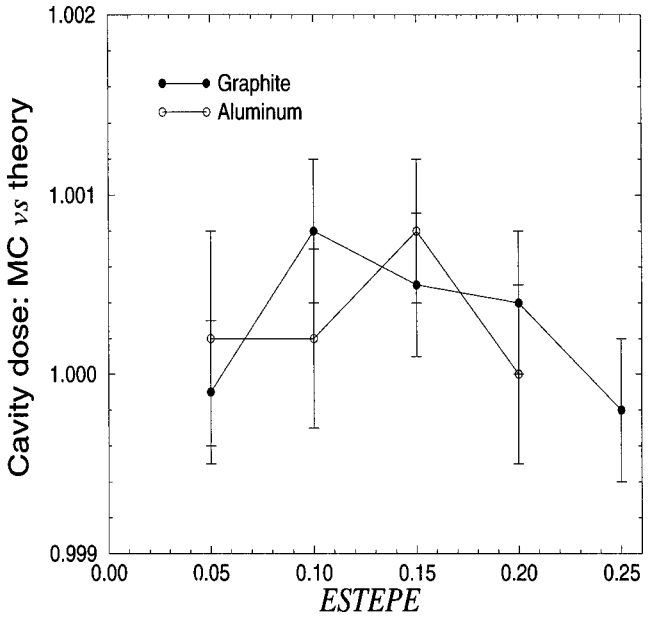

FIG. 10. The ratio of the simulated cavity dose to the theoretically known dose as a function of the maximum fractional energy loss per step calculated with EGSnrc. Particle production thresholds were AE=521 keV, AP=10 keV.

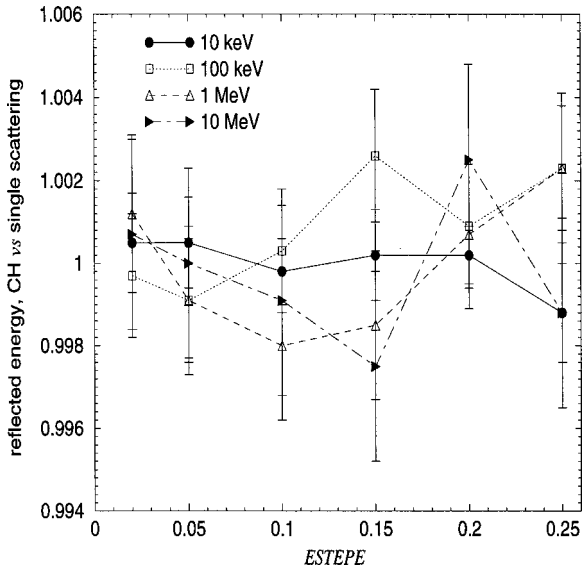

FIG. 11. The ratio of the energy fraction reflected on a semi-infinite water surface, calculated using CH simulation with EGSnrc, to the reflected energy fraction calculated using a single scattering simulation. Results are shown as a function of the maximum energy loss fraction per step in the CH simulations.

tering mode for a statistical accuracy of better than 0.2%), all other simulations were with secondary particle creation taken into account. The CH results show no step-size variation and are consistent with the single scattering simulations within the statistical accuracy (0.1% at 10 keV, 0.15% at 100 keV, 0.18% at 1 MeV, and 0.23% at 10 MeV).

IV. SUMMARY

The EGSnrc system presented in this paper incorporates the following improvements compared to EGS4/PRESTA.

(i) The exact multiple scattering theory of Ref. 11 that is based on the screened Rutherford cross section, together with improved treatment of energy loss discussed in Sec. II A and Appendix A.

(ii) The electron-step algorithm of Ref. 17, which is shown to reproduce first- and second-order spatial moments to within 0.1%, once the energy loss corrections derived in Appendix B are taken into account.

(iii) An exact boundary crossing algorithm via analog modeling of elastic scattering in the vicinity of boundaries.

(iv) An improved evaluation of energy loss due to subthreshold processes.

(v) A correct implementation of the fictitious cross section method for sampling distances between discrete interactions.

It is demonstrated that with these improvements, an artifact-free condensed history simulation of ion chamber response is possible on the 0.1% level if the limitations of the underlying algorithms are well understood and the appropriate step-size restrictions taken into account ($\xi \leqslant 0.5$, ESTEPE $\leqslant 0.25$). Note that this is the accuracy of the implementation of the condensed history technique. This is not the same as the overall accuracy, which is affected by the accuracy of the underlying cross sections.

ACKNOWLEDGMENTS

Partial financial support for this work has been provided by the German Research Society (Deutsche Forschungsgemeinschaft), Contract No. KA 1298/1-1. I am grateful to D. W. O. Rogers and J. P. Seuntjens of NRCC for many useful suggestions on the manuscript. A. F. Bielajew, University of Michigan, is acknowledged for providing an early version of the new ELECTR routine.

APPENDIX A: IMPROVED MODELING OF ENERGY LOSS IN THE MULTIPLE SCATTERING DISTRIBUTION

Generally, the MS distribution for an initial energy E and a pathlength s is a function of E, s, the material where the transport takes place and the scattering angle. If energy loss is neglected and elastic scattering described by the screened Rutherford cross section, the material dependence can be eliminated and the probability for scattering by a given angle represented as a function of two parameters; the pathlength s and the screening angle χ_a. Applying suitable variable transformations, the dependence on s and χ_a can be strongly reduced and the MS angle sampled from a relatively small database of precalculated data for arbitrary pathlengths and screening angles. This was demonstrated in Ref. 11. Energy loss was taken into account in Ref. 11 by approximating the G_l's [see Eq. (3)] with

$$G_l \approx \kappa_l(\tilde{E})s\left[1+\frac{4+6\tilde{\tau}+3\tilde{\tau}^2}{3(2+\tilde{\tau})^2}\frac{\epsilon^2}{(2-\epsilon)^2}\right]. \tag{A1}$$

Here, $\tilde{E}=E_i-\Delta E/2$ denotes the average electron energy, $\epsilon=\Delta E/E_i$ the energy loss fraction, and $\tilde{\tau}=\tilde{E}/m$ the average energy in units of the electron's rest energy m. Equation (A1) follows from the more general equation,

$$G_l \approx \frac{\kappa_l(\tilde{E})}{L(\tilde{E})}\Delta E + \frac{2\kappa_l(\tilde{E})L'(\tilde{E})^2 + \kappa_l''(\tilde{E})L(\tilde{E})^2 - L(\tilde{E})[2\kappa_l'(\tilde{E})L'(\tilde{E}) + \kappa_l(\tilde{E})L''(\tilde{E})]}{L(\tilde{E})^3}\frac{\Delta E^3}{24} + \cdots, \tag{A2}$$

which is the result of the application of Euler's integration formula [see Eq. (16)], together with various approximations for the first- and second-order derivatives of κ_l and L with respect to E, κ_l', κ_l'' and L',L''. Because in the no-energy loss case the G_l's are given by $G_l = \kappa_l s$, the no-energy loss distribution can be employed to sample the MS angle using an ''effective'' pathlength of s times the term in the square brackets in Eq. (A1).

An improvement compared to this approach can be achieved as follows. First, an ''effective'' energy E_{eff} for which $G_2/G_1 = \kappa_2(E_{\text{eff}})/\kappa_1(E_{\text{eff}})$ is determined. Then the no energy loss MS distribution of Ref. 11 for a pathlength $s_{\text{eff}} = G_1/\kappa_1(E_{\text{eff}}) = G_2/\kappa_2(E_{\text{eff}})$ is used. That is, the moments G_l are approximated by

$$G_l \approx \kappa_l(E_{\text{eff}})s_{\text{eff}}, \tag{A3}$$

achieving in this way that G_1 and G_2 are exactly reproduced. Simple calculation shows that

$$\begin{aligned} E_{\text{eff}} &= E_i - \frac{\Delta E}{2} + \frac{\Delta E^2}{24} \\ &\quad \times \left(\frac{\kappa_1''(\tilde{E})\kappa_2(\tilde{E}) - \kappa_1(\tilde{E})\kappa_2''(\tilde{E})}{\kappa_1'(\tilde{E})\kappa_2(\tilde{E}) - \kappa_1(\tilde{E})\kappa_2'(\tilde{E})} - 2\frac{L'(\tilde{E})}{L(\tilde{E})} \right) \\ &\quad + O(\Delta E^3), \\ s_{\text{eff}} &= s\left(1 - \frac{\kappa_1'(\tilde{E})\kappa_2''(\tilde{E}) - \kappa_1''(\tilde{E})\kappa_2'(\tilde{E})}{\kappa_1(\tilde{E})\kappa_2'(\tilde{E}) - \kappa_1'(\tilde{E})\kappa_2(\tilde{E})}\frac{\Delta E^2}{24} + O(\Delta E^4) \right), \end{aligned} \tag{A4}$$

satisfies the above requirements. Remarkably, the correction in s_{eff} does not depend on the stopping power but only on the elastic scattering properties of the material. The dependence of E_{eff} on the stopping power via L'/L is also rather weak.

Note that the above equations are valid for any single elastic scattering cross section. Their general applicability depends on a possible near-cancellation of the denominator. A detailed discussion of this issue for more accurate elastic scattering cross sections goes beyond the purpose of this paper. Here, we give the resulting expressions for the screened Rutherford cross section, which is the basis of the multiple scattering theory under investigation. We have

$$\begin{aligned} \kappa_1 &= \frac{\chi_{cc}^2}{2p^2\beta^2}\left[\ln\left(1 + \frac{4b_c p^2}{\chi_{cc}^2}\right)\left(1 + \frac{\chi_{cc}^2}{4b_c p^2}\right) - 1 \right], \\ \kappa_2 &= 3\frac{\chi_{cc}^2}{2p^2\beta^2}\left[\ln\left(1 + \frac{4b_c p^2}{\chi_{cc}^2}\right)\left(1 + \frac{\chi_{cc}^2}{2b_c p^2}\right) - 2 \right] \\ &\quad \times \left(1 + \frac{\chi_{cc}^2}{4b_c p^2}\right), \end{aligned} \tag{A5}$$

where p is the particle momentum and b_c and χ_{cc} material dependent constants (see, e.g., Ref. 3 for their definition). With this the expressions for E_{eff} and s_{eff} simplify to

$$\begin{aligned} E_{\text{eff}} &= E_i\left[1 - \frac{\epsilon}{2} - \frac{\epsilon^2}{12(2-\epsilon)}\left(\frac{5\tilde{\tau}^2 + 10\tilde{\tau} + 6}{(\tilde{\tau}+1)(\tilde{\tau}+2)} + 2b(\tilde{E}) \right) \right. \\ &\quad \left. + O(\epsilon^3) \right], \\ s_{\text{eff}} &= s\left(1 - \frac{\epsilon^2}{3(2-\epsilon)}\frac{\tilde{\tau}^4 + 4\tilde{\tau}^3 + 7\tilde{\tau}^2 + 6\tilde{\tau} + 4}{(\tilde{\tau}+1)^2(\tilde{\tau}+2)^2} + O(\epsilon^4) \right), \end{aligned} \tag{A6}$$

where we have defined

$$b(E) = \frac{E}{C(E)}\frac{\mathrm{d}C(E)}{\mathrm{d}E}, \quad C(E) = L(E)\beta^2, \tag{A7}$$

β denoting the particle velocity in units of the speed of light. Note that $C(E)$ is a rather slowly (logarithmically) varying function of energy and therefore $b(E)$ is small for all energies large compared to the mean ionization energy.

APPENDIX B: ENERGY LOSS CORRECTIONS TO THE ELECTRON-STEP ALGORITHM OF REF. 17

As mentioned in Sec. II B, the parameters of the electron-step algorithm were derived in Ref. 17, neglecting energy loss. Here, we will give corrections that are necessary for an accurate CH simulation of electron transport.

To outline the approach, we will consider the average transport distance in the initial direction of motion, $\langle z \rangle$, and the average lateral deflection squared, $\langle r^2 \rangle$. From the theory of Lewis,[13] we have

$$\begin{aligned} \langle z \rangle &= \int_0^s \mathrm{d}s'\, k_1(s'), \\ \langle r^2 \rangle &= \frac{4}{3}\int_0^s \mathrm{d}s' \int_0^{s'} \mathrm{d}s''\, k_1(s'-s'')[1 - k_2(s'')], \end{aligned} \tag{B1}$$

where k_i is defined in Eq. (3). Neglect of energy loss corresponds to the approximation $k_i(s') = \exp(-G_i s'/s)$, which gives

$$\begin{aligned} \langle z \rangle &\approx \langle \tilde{z} \rangle \equiv s\frac{1 - \exp(-\xi)}{\xi} \approx s\left(1 - \frac{\xi}{2} + \frac{\xi^2}{6} \pm \cdots \right), \\ \langle r^2 \rangle &\approx \langle \tilde{r}^2 \rangle \equiv s^2\frac{4}{3\xi}\left(1 - \frac{\gamma}{\gamma - 1}\frac{1 - \exp(-\xi)}{\xi} \right. \\ &\quad \left. + \frac{1}{\gamma - 1}\frac{1 - \exp(-\gamma\xi)}{\gamma\xi} \right) \\ &\approx s^2\left(\frac{2\gamma}{9}\xi - \frac{\gamma(\gamma+1)}{18}\xi^2 \pm \cdots \right), \end{aligned} \tag{B2}$$

where ξ and γ are defined in Sec. II B and the over tilde in $\langle\tilde{z}\rangle$ and $\langle\tilde{r}^2\rangle$ indicates that these quantities result from the neglect of energy loss. A straightforward but rather lengthy calculation yields

$$\begin{aligned}\langle z\rangle &= s\left[1-\frac{\xi}{2}\left(1+\frac{\kappa_1'(\tilde{E})}{\kappa_1(\tilde{E})}\frac{\Delta E}{6}+O(\Delta E^2)\right)\right.\\ &\quad\left.+\frac{\xi^2}{6}\left(1+\frac{\kappa_1'(\tilde{E})}{\kappa_1(\tilde{E})}\frac{\Delta E}{4}+O(\Delta E^2)\right)\pm\cdots\right],\\ \langle r^2\rangle &= s^2\left[\frac{2\gamma}{9}\xi\left(1+\frac{\kappa_2'(\tilde{E})}{\kappa_2(\tilde{E})}\frac{\Delta E}{4}+O(\Delta E^2)\right)\right.\\ &\quad-\frac{\gamma^2}{18}\xi^2\left(1+\frac{\kappa_2'(\tilde{E})}{\kappa_2(\tilde{E})}\frac{2\,\Delta E}{5}+O(\Delta E^2)\right)\\ &\quad-\frac{\gamma}{18}\xi^2\left\{1+\left(3\frac{\kappa_2'(\tilde{E})}{\kappa_2(\tilde{E})}-\frac{\kappa_1'(\tilde{E})}{\kappa_1(\tilde{E})}\right)\frac{\Delta E}{10}+O(\Delta E^2)\right\}\\ &\quad\left.\pm\cdots\right].\end{aligned}\tag{B3}$$

The following expressions for the moments $\langle z\rangle$ and $\langle r^2\rangle$ result from the algorithm given by Eq. (5):

$$\begin{aligned}\langle z\rangle &= \langle a_1\rangle+\tfrac{2}{3}\exp(-\xi/2)+\langle a_2\rangle\exp(-\xi),\\ \langle r^2\rangle &= \frac{1-\exp(-\gamma\xi/2)}{3}\{\delta^2+(1-\delta)^2[1+\exp(-\gamma\xi/2)]\}\\ &\quad+\frac{2\langle a_2^2\rangle}{3}[1-\exp(-\gamma\xi)]\\ &\quad\times\frac{\exp(-\xi/2)[1-\exp(-\gamma\xi/2)]}{9}.\end{aligned}\tag{B4}$$

Comparing Eqs. (B2)–(B4) it is easy to see that the parameters a_1, a_2, and δ should be corrected according to

$$a_1\to a_1(1+\alpha_1),\quad a_2\to a_2(1-\alpha_1),\quad \delta\to\delta+\alpha_2,\tag{B5}$$

with

$$\begin{aligned}\alpha_1 &= -\frac{\kappa_1'(\tilde{E})}{\kappa_1(\tilde{E})}\frac{\Delta E}{2}+O(\Delta E^2),\\ \alpha_2 &= \left(\frac{\kappa_2'(\tilde{E})}{\kappa_2(\tilde{E})}-\frac{\kappa_1'(\tilde{E})}{\kappa_1(\tilde{E})}\right)\frac{\Delta E}{2\sqrt{6}}+O(\Delta E^2).\end{aligned}\tag{B6}$$

The above equations yield for the screened Rutherford cross section [κ_1 and κ_2 given in Eq. (A5)],

$$\begin{aligned}\alpha_1 &\approx \left(\frac{2+2\tilde{\tau}+\tilde{\tau}^2}{(1+\tilde{\tau})}-\frac{1+\tilde{\tau}}{\ln(1+4/\tilde{\chi}_a^2)[(1+\tilde{\chi}_a^2/4)-1]}\right)\frac{\Delta E/\tilde{E}}{(2+\tilde{\tau})},\\ \alpha_2 &\approx \frac{\Delta E/\tilde{E}}{\sqrt{6}(1+\tilde{\tau})(2+\tilde{\tau})\{\ln(1+4/\tilde{\chi}_a^2)[(1+\tilde{\chi}_a^2/4)-1]\}\{\ln(1+4/\tilde{\chi}_a^2)[1+\tilde{\chi}_a^2/2)-2]\}},\end{aligned}\tag{B7}$$

where $\tilde{\chi}_a^2=\chi_{cc}^2/[b_c\tilde{E}(\tilde{E}+2m)]$ is the midpoint screening angle, $\tilde{\tau}=\tilde{E}/m$ the midpoint energy in units of the rest energy of the electron and we have neglected some small terms proportional to $\tilde{\chi}_a^2$.

APPENDIX C: THE FICTITIOUS CROSS SECTION METHOD

In this appendix we give a proof that the fictitious cross section method yields the correct interaction probability distribution between subsequent collisions, if certain criteria are met, and helps understand why the modification proposed by Ma and Nahum[20] is biased.

Let denote by Σ_0 the cross section used to sample distances between discrete interactions,

$$\Sigma_0=\Sigma(s)+\Sigma_f(s)\equiv\text{const.}\tag{C1}$$

Here, $\Sigma(s)$ is the cross section for a real interaction and $\Sigma_f(s)$ the cross section for a ''fictitious'' interaction that leaves the energy and direction of the particle unchanged. Note that the s dependence of the cross sections expresses the dependence on both the material (which may change before reaching the next interaction site) and the energy (which decreases with pathlength traveled in a condensed history simulation of electron transport). Once at the interaction site, a real collision takes place with the probability

$$w(s)=\frac{\Sigma(s)}{\Sigma_0}.\tag{C2}$$

The probability distribution that exactly one interaction (real or fictitious) takes place in the interval ds_1 around s_1 is

$$\begin{aligned}p_1(s_1) &= \Sigma_0\exp(-\Sigma_0 s_1)\exp[-\Sigma_0(s-s_1)]\\ &= \exp(-\Sigma_0 s)\Sigma_0\end{aligned}\tag{C3}$$

(the probability that an interaction occurs at s_1 times probability that no further interactions take place in the range $s_1\cdots s$). In an analogous manner we have for the probability distribution that exactly n interactions take place in the intervals ds_1, $ds_2,\ldots,ds_n$ around s_1, $s_2,\ldots,s_n$,

$$p_n(s_1,\ldots,s_n)=\Sigma_0\exp(-\Sigma_0 s_1)\Sigma_0\Theta(s_2-s_1)\times\exp[-\Sigma_0(s_2-s_1)]\cdots\Sigma_0\Theta(s_n-s_{n-1})\times\exp[-\Sigma_0(s_n-s_{n-1})]\exp[-\Sigma_0(s-s_n)]=\exp(-\Sigma_0 s)\Sigma_0^n, \tag{C4}$$

where Θ is the Heaviside step function that is used to assure that $s_{k+1}\geqslant s_k$. The probability that a particle did not have a real interaction after n collisions (real or fictitious) is

$$\overline{c}_n(s_1,\ldots,s_n)=\prod_{k=1}^{n}[1-w(s_k)]. \tag{C5}$$

Therefore, the probability that no real interaction took place after a pathlength of s is

$$P(s)=\sum_{n=0}^{\infty}\int\left(\prod_{k=1}^{n}\mathrm{d}s_k\right)p_n(s_1,\ldots,s_n)\tilde{c}_n(s_1,\ldots,s_n)=\exp(-\Sigma_0 s)\sum_{n=0}^{\infty}\tilde{I}_n, \tag{C6}$$

where

$$\tilde{I}_n=\int_0^s\mathrm{d}s_1[\Sigma_0-\Sigma(s_1)]\int_{s_1}^s\mathrm{d}s_2[\Sigma_0-\Sigma(s_2)]\cdots\times\int_{s_{n-1}}^s\mathrm{d}s_n[\Sigma_0-\Sigma(s_n)] \tag{C7}$$

($\tilde{I}_0=1$). Using $n-1$ times partial integration, we have

$$\tilde{I}_n=\frac{1}{n!}\left[\int_0^s\mathrm{d}s'[\Sigma_0-\Sigma(s')]\right]^n, \tag{C8}$$

and therefore

$$P(s)=\exp\left(-\int_0^s\mathrm{d}s'\,\Sigma(s')\right). \tag{C9}$$

This completes the proof. A crucial condition for the correctness of the above derivation is that $w(s)\leqslant 1$, i.e.;

$$\Sigma_0\geqslant\Sigma(s),\quad\text{for all } s. \tag{C10}$$

The derivation given above is also useful for examining the correctness of the approach proposed by Ma and Nahum.[20] They suggest that, for a step beginning at $s=s'$, $f_{\mathrm{MFP}}(s')\Sigma(s')$ should be used to sample the transport distance to the next discrete interaction. From the above discussion it is apparent that

$$f_{\mathrm{MFP}}(s')\geqslant\frac{\Sigma_{\max}}{\Sigma(s')}, \tag{C11}$$

should be used, where $\Sigma_{\max}$ is the maximum of the cross section. With $f_{\mathrm{MFP}}(s')=\Sigma_0/\Sigma(s')$, $\Sigma_0\geqslant\Sigma_{\max}$, we will have then the same approach as described at the beginning of this appendix. The problem arrives from their rejection criterion, which is

$$w(s'')=\frac{\Sigma(s'')+\Sigma(s')}{2f_{\mathrm{MFP}}(s')\Sigma(s')}=\frac{\Sigma(s'')+\Sigma(s')}{2\Sigma_0}. \tag{C12}$$

Performing the same calculation for this interaction probability we arrive at the discrete interaction distribution that follows from the modification by Ma and Nahum, $P_{\mathrm{MN}}(s)$,

$$P_{\mathrm{MN}}(s)=\exp\left(-\int_0^s\mathrm{d}s'\frac{\Sigma(s=0)+\Sigma(s')}{2}\right). \tag{C13}$$

Clearly, sampling distances between discrete interactions from the above distribution will overestimate (underestimate) their average number if the cross section is decreasing (increasing) with s. On the other side, if the cross section is large so that the average pathlength between a discrete interaction is short, the bias may be rather small.

APPENDIX D: ACCURATE EVALUATION OF ENERGY LOSS INTEGRALS

To obtain a better estimate of ΔE in Eq. (20), we use an expansion of $L(E)$ around the initial energy E_i,

$$L(s')\approx L(s=0)+\left.\frac{\mathrm{d}L(s)}{\mathrm{d}s}\right|_{s=0}s'+\left.\frac{\mathrm{d}^2L(s)}{\mathrm{d}s^2}\right|_{s=0}\frac{s'^2}{2}=L(E_i)\left[1-L'(E_i)s'+[L'(E_i)^2+L(E_i)L''(E_i)]\frac{s'^2}{2}\right], \tag{D1}$$

L' and L'' denoting the first- and second-order derivatives of L with respect to E, to arrive at

$$\int_0^s\mathrm{d}s'\,L[E(s')]\approx\Delta E_1\left[1+\frac{1}{(1+\tau_i)(2+\tau_i)}\epsilon_1+\frac{2+2\tau_i+\tau_i^2}{(1+\tau_i)^2(2+\tau_i)^2}\epsilon_1^2-b\,\epsilon_1\left(\frac{1}{2}+\frac{2}{3}\frac{\epsilon_1}{(1+\tau_i)(2+\tau_i)}+(1-b)\frac{\epsilon_1}{6}\right)\right]\equiv\Delta E_2, \tag{D2}$$

where $\Delta E_1=L(E_i)s$, $\tau_i=E_i/m$, $\epsilon_1=\Delta E_1/E_i$ and $b=b(E_i)$, $b(E)$ defined in Eq. (A7). Note that ΔE_2, being already more accurate than PRESTA's approach (see Fig. 7), can be calculated from the stopping power at the beginning of the step, saving in this way the evaluation of a logarithm (logarithmic interpolation is used in EGS4 to calculate energy-dependent quantities). A subsequent reevaluation of the integral with $L(E)$ expanded around $E_i-\Delta E_2/2$ (i.e., the application of Euler's integration formula) yields

$$\int_0^s\mathrm{d}s'\,L[E(s')]\approx\frac{L(E_i-\Delta E_2/2)s}{g[E_i-\Delta E_2/2,L(E_i-\Delta E_2/2)s/E_i]}\equiv\Delta E_3, \tag{D3}$$

where g is defined in Eq. (19). Finally, a correction for the difference between ΔE_2 and ΔE_3 is applied:

$$\int_0^s \mathrm{d}s'\, L[E(s')] \approx \Delta E_3\left(1+\frac{b}{2}(\epsilon_2-\epsilon_3)\right)\left(1-x+\frac{4+6\tau_2+3\tau_2^2}{4}x^2\right), \tag{D4}$$

$$x=\frac{\epsilon_2-\epsilon_3}{(1-\epsilon_2/2)(1+\tau_2)(2+\tau_2)}, \quad \epsilon_2=\frac{\Delta E_2}{E_i},$$

$$\epsilon_3=\frac{\Delta E_3}{E_i}, \quad \tau_2=\frac{E_i-\Delta E_2/2}{m}.$$

[1] M. J. Berger, ''Monte Carlo calculation of the penetration and diffusion of fast charged particles, in *Methods in Computational Physics*, edited by B. Alder, S. Fernbach, and M. Rotenberg (Academic, New York, 1963), Vol. 1, pp. 135–215.

[2] A. F. Bielajew and D. W. O. Rogers, ''Electron step-size artefacts and PRESTA,'' in *Monte Carlo Transport of Electrons and Photons*, edited by T. M. Jenkins, W. R. Nelson, A. Rindi, A. E. Nahum, and D. W. O. Rogers (Plenum, New York, 1988), pp. 115–137.

[3] W. R. Nelson, H. Hirayama, and D. W. O. Rogers, ''The EGS4 code system,'' Report No. SLAC-265, Stanford Linear Accelerator Center, Stanford, California, 1985.

[4] S. M. Seltzer, ''An overview of ETRAN Monte Carlo methods,'' in Ref. 2, pp. 153–182.

[5] J. A. Halbleib, R. P. Kensek, T. A. Mehlhorn, G. D. Valdez, S. M. Seltzer, and M. J. Berger, ''ITS Version 3.0: The integrated TIGER series of coupled electron/photon Monte Carlo transport codes,'' Sandia Report, No. SAND91-1634, 1992.

[6] J. F. Briesmeister, MCNP—A general Monte Carlo *N*-particle transport code, ''Los Alamos National Laboratory Report, No. LA-12625-M,'' Los Alamos, NM, 1993.

[7] A. F. Bielajew, D. W. O. Rogers, and A. E. Nahum, ''Monte Carlo simulation of ion chamber response to ^{60}Co—Resolution of anomalies associated with interfaces,'' Phys. Med. Biol. **30**, 419–428 (1985).

[8] S. A. Goudsmit and J. L. Saunderson, ''Multiple scattering of electrons,'' Phys. Rev. **57**, 24–29 (1940).

[9] S. A. Goudsmit and J. L. Saunderson, ''Multiple scattering of electrons. II,'' Phys. Rev. **58**, 36–42 (1940).

[10] M. J. Berger and R. Wang, ''Multiple-scattering angular deflections and energy-loss straggling,'' in Ref. 2, pp. 21–56.

[11] I. Kawrakow and A. F. Bielajew, ''On the representation of electron multiple elastic-scattering distributions for Monte Carlo calculations,'' Nucl. Instrum. Methods **134B**, 325–336 (1998).

[12] I. Kawrakow, ''On the condensed history technique for the simulation of electron elastic scattering,'' Radiat. Phys. Chem. **53**, 345–352 (1997).

[13] H. W. Lewis, ''Multiple scattering in an infinite medium,'' Phys. Rev. **78**, 526–529 (1950).

[14] L. Eyges, ''Multiple scattering with energy loss,'' Phys. Rev. **74**, 1534 (1948).

[15] A. F. Bielajew and D. W. O. Rogers, ''PRESTA: The parameter reduced electron-step transport algorithm for electron Monte Carlo transport,'' Nucl. Instrum. Methods Phys. Res. B **18**, 165–181 (1987).

[16] I. Kawrakow, ''Electron transport: longitudinal and lateral correlation algorithm,'' Nucl. Instrum. Methods Phys. Res. B **114**, 307–326 (1996).

[17] I. Kawrakow and A. F. Bielajew, ''On the condensed history technique for electron transport,'' Nucl. Instrum. Methods **142B**, 253–280 (1998).

[18] E. W. Larsen, ''A theoretical derivation of the condensed history algorithm,'' Ann. Nucl. Energy **19**, 701–714 (1992).

[19] D. W. O. Rogers, ''Low energy electron transport with EGS,'' Nucl. Instrum. Methods **227**, 535–548 (1984).

[20] C. M. Ma and A. E. Nahum, ''A new algorithm for EGS4 low-energy electron transport to account for the change in discrete interaction cross-section with energy,'' Nucl. Instrum. Methods Phys. Res. B **72**, 319–330 (1992).

[21] B. J. Foote and V. G. Smyth, ''The modelling of electron multiple-scattering in EGS4/PRESTA and its effect on ionization-chamber response,'' Nucl. Instrum. Methods Phys. Res. B **100**, 22–30 (1995).

[22] A. E. Nahum, ''Simulation of dosimeter response and interface effects,'' in Ref. 2, pp. 523–547.

[23] D. W. O. Rogers, ''How accurately can EGS4/PRESTA calculate ion chamber response?,'' Med. Phys. **20**, 319–323 (1993).